Identification of primary and secondary resonances: experimental continuation and broadband data-based modeling

Nonlinear Dynamics (2026)114:81
https://doi.org/10.1007/s11071-025-11940-4

RESEARCH

Identification of primary and secondary resonances: experimental continuation and broadband data-based modeling

D. Anastasio[1] · G. Raze[2] · S. Marchesiello[1] · G. Kerschen[2]

Received: 3 February 2025 / Revised: 9 September 2025 / Accepted: 1 November 2025

Abstract
This paper presents a comparative study of two sets of techniques for identifying primary and secondary resonances in nonlinear dynamic systems: experimental continuation and broadband data-based modeling. The former refers to methods integrating control and continuation processes to empirically derive the bifurcation diagram of a nonlinear system. These approaches do not require a model, but the need for a controller introduces complexity in the experiments. Conversely, broadband data-based modeling uses wide-spectrum excitation data to develop a nonlinear model of the system. Proper model validation is crucial in this process to ensure accurate results. In this work, the comparison is carried out using two different setups: an electronic Duffing system and a thin-walled nonlinear beam. The findings demonstrate that both methods, when properly applied, can effectively identify not only primary resonances, but also the more challenging secondary ones. Measuring and predicting these resonances constitutes an ambitious task for data-based approaches. Moreover, the direct comparison between experimental continuation and broadband data-based techniques highlights the complementary strengths and limitations of each approach, providing new insights and perspectives on the identification of nonlinear resonances.

Keywords Nonlinear system identification · Experimental continuation · Broadband · Duffing · Thin-walled

1 Introduction

Understanding and predicting the behavior of nonlinear mechanical systems has become an important aspect of structural engineering research in recent decades. Nonlinearity may manifest as an inherent characteristic, requiring numerical or experimental characterization, or it may be intentionally exploited in a design process to take advantage of phenomena inaccessible to linear systems [1, 2].

In this context, the development of nonlinear models directly from measured data has become a widely adopted approach, since it enables the inference of a mathematical representation of the measured phenomena with limited dependence on prior information about the system. Referred to as "nonlinear system identification", this approach has led to the development of numerous techniques to manage increasing system complexity and experimental challenges [3, 4]. Despite significant advancements in this field, nonlinear system identification remains a demanding process and presents difficulties and constraints to researchers. For instance, the nonlinearity must be properly excited and measured, and a prior characterization stage is often necessary to select a feasible model structure. Once identified and validated, the nonlinear model can serve various purposes: gaining insights into the underlying physical phenomena and their interactions, predicting the behavior of the system, and supporting control or design strategies. Specifically, this paper focuses on the study of periodic solutions in nonlinear systems. This represents a central topic in nonlinear dynamics and, in particular, in the field of mechanical systems considered in this work, as it serves as the cornerstone of resonance phenomena, harmonic generation, and bifurcation analysis [5].

✉ D. Anastasio
dario.anastasio@polito.it

[1] Department of Mechanical and Aerospace Engineering, Politecnico Di Torino, Turin, Italy

[2] Aerospace and Mechanical Engineering Department, University of Liège, Liège, Belgium

Published online: 08 January 2026

Recently, subspace-based identification methods have been employed for this purpose [6, 7] by merging broadband data-based modeling and numerical continuation techniques [8]. Specifically, the approach presented in [7] combines the time-domain nonlinear subspace identification method (NSI) [9] with a dedicated formulation of the harmonic balance (HB) method [8, 10]. This allows to estimate the nonlinear frequency response curves (NFRCs) of the system under study and to track its bifurcations. The method is referred to as HB-NSI and requires input–output testing under wide spectrum excitation in an open-loop setting. It is worth noting that this approach can handle multiple modes simultaneously, since a broadband excitation is employed in the identification stage. In [11], this method has been employed to estimate the NFRCs of a geometrically nonlinear beam across different resonances. In this context, frequency responses are predicted by the identified model rather than obtained directly from experiments.

A model-less alternative to this approach that has recently emerged in the scientific community is the adoption of experimental continuation techniques. The first method to accomplish this purpose is called control-based continuation (CBC) [12] and mirrors the pseudo-arclength numerical continuation. Its primary limitation is the need to calculate derivatives from experimental data, which has been addressed in more recent techniques, such as simplified CBC (SCBC) [13], phase-locked loops (PLL) [14], and response-controlled testing (RCT) [15]. Generally, the base requirement of these methods is to have one or more feedback control loops, which demand adequate instrumentation and an iterative test procedure. Furthermore, the interaction with the shaker [14] and the presence of harmonics in the input spectrum [16] are two aspects that must be accounted for. Despite the experimental difficulties, this class of methods has the advantage of directly measuring NFRCs, as well as backbone curves [16], unstable branches [17] and nonlinear normal modes [14]. A recent development in control-based continuation methods is the so-called arclength CBC (ACBC), which introduces a derivative-free approach to experimental arclength continuation [18, 19]. We also note that there have been a few attempts recently to merge the framework of experimental continuation with system identification to obtain a parametric representation of the system [20, 21].

Recent comparative studies [22, 23] have focused on primary (or fundamental) resonances in nonlinear structures, evaluating the black-box broadband identification method PNLSS (Polynomial Nonlinear State Space) [24] and near-resonant models based on PLL [25]. In contrast, the present work provides novel and more comprehensive perspectives into the use of broadband data-based modeling and experimental continuation by including both primary and secondary resonances. While the analysis of primary resonances represents a standard approach in nonlinear structural dynamics, the investigation of secondary resonances introduces additional experimental challenges. An $m:l$ resonance occurs when nonlinear interactions cause the system to respond predominantly at a frequency ratio m/l of the fundamental excitation, with m and l positive integers, often leading to complex vibration patterns. Like primary resonances, secondary ones can also lead to large-amplitude motion, which can be detrimental to structural integrity [1, 19]. The most common case of superharmonic resonance corresponds to $m:1, m>1$. Owing to their complexity, secondary resonances provide a meaningful benchmark for assessing the limitations of the methods considered here: HB-NSI for broadband data-based modeling, and ACBC and PLL for experimental continuation. To this end, two experimental setups are considered: an electronic Duffing system and a thin-walled nonlinear beam. The electronic Duffing system is a circuit designed to emulate the behavior of a Duffing oscillator [26]. It features adjustable controls for tuning system parameters, making it a suitable single-degree-of-freedom benchmark for nonlinear dynamical techniques. Further details on this circuit can be found in [27]. To extend the comparison to multimodal structures, a clamped–clamped thin-walled beam is also considered. In this case, geometrical nonlinearity arises when the beam undergoes large-amplitude vibrations, resulting in a distributed nonlinear strain–displacement relation [1]. The study focuses on the first four modes of the structure.

The two approaches considered in this work are fundamentally different in spirit, yet both provide efficient means to empirically understand the nonlinear dynamic phenomena in structures. This comparative analysis offers valuable insights into the strengths and weaknesses of each method, while also serving as mutual validation.

2 Methods

2.1 Experimental continuation

The two experimental continuation approaches used in this work, ACBC and PLL, aim to directly measure NFRCs, including their unstable parts. The stabilization of these unstable orbits is achieved thanks to feedback control. These methods are briefly presented hereafter.

ACBC works along the principles of CBC, wherein the structure is excited by the output of a proportional-derivative (PD) controller. A block-diagram representation of the ACBC approach is given in Fig. 1a. The force acting on the structure is

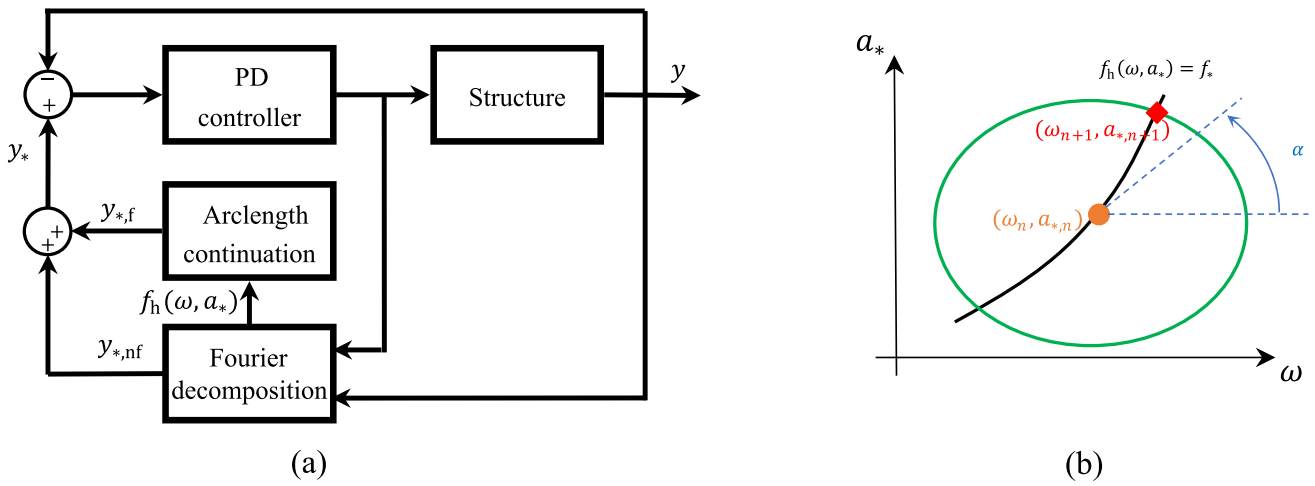

Fig. 1 ACBC schematics (**a**) and representation of the derivative-free arclength continuation procedure (**b**)

$$f(t) = k_{d,y}(\dot{y}_*(t) - \dot{y}(t)) + k_{p,y}(y_*(t) - y(t)), \quad (1)$$

where $k_{d,y}$ and $k_{p,y}$ are the differential and proportional gains of the controller, respectively. This controller can stabilize an equilibrium whose measured output, $y(t)$, is close to a target signal $y_*(t)$. Since the goal of the test is to measure an NFRC, this target signal is adjusted to make the control non-invasive. In other words, it is adjusted to make an equilibrium of the closed-loop system identical to that of the open-loop system. This is ensured if the output of the controller is equal to the desired excitation profile when the structure is on one of its periodic orbits. In most cases, this desired excitation is a harmonic one with prescribed amplitude f_*.

ACBC secures non-invasiveness in two main steps by working on the reference signal, which is split into its fundamental and non-fundamental harmonics

$$y_*(t) = y_{*,f}(t) + y_{*,nf}(t) = a_* \sin(\omega t) + y_{*,nf}(t), \quad (2)$$

where a_* is the fundamental harmonic amplitude, and ω the angular frequency of excitation. First, the non-fundamental harmonics of the target signal $y_{*,nf}(t)$ are set to be equal to those of the response using an online Fourier decomposition of $y(t)$ with adaptive filters [17]. For primary resonances, this guarantees that the excitation remains harmonic since the signal $y_{*,f}(t) + y_{*,nf}(t) - y(t)$ is harmonic as well (neglecting the higher harmonics that are not included in the online Fourier decomposition). In the case of secondary resonances, however, this procedure is less straightforward and prone to fail [19]; this issue and its implications are further discussed in Sect. 3.3. In the second step, since an NFRC is the response of the structure under test at a given forcing amplitude, the fundamental harmonic $y_{*,f}(t)$ is tailored to apply the desired excitation amplitude to the structure. a_* and ω are adjusted to find a one-dimensional manifold defined by $f_h(\omega, a_*) = f_*$, where $f_h(\omega, a_*)$ is the harmonic forcing amplitude applied to the structure. This problem is solved using a derivative-free arclength continuation algorithm. An ellipse is defined around a current point $(\omega_n, a_{*,n})$, assumed to lie on the NFRC, as

$$\omega(\alpha) = \omega_n + \Delta\omega \cos(\alpha), a_*(\alpha) = a_{*,n} + \Delta a_* \sin(\alpha), \quad (3)$$

where $\Delta\omega$ and Δa_* are the semi-axes of the ellipse. The angle α is then automatically adjusted by the integral law with integral gain $k_{\alpha,i}$

$$\dot{\alpha} = k_{\alpha,i}(f_* - f_h(\omega, a_*)) \quad (4)$$

until $f_h(\omega, a_*) - f_* = 0$ (up to some tolerance), which signals a point on the NFRC. Figure 1b schematically represents this procedure. By recentering the ellipse on this newfound point and repeating the procedure, the NFRC can be determined point by point. More details about ACBC are given in [18, 19].

The second approach, PLL, explicitly parametrizes the response curve by the phase shift θ between the forcing and one harmonic of the response. Near a resonance, the latter can locally parametrize an NFRC, unlike the frequency of excitation [28]. This parametrization is realized thanks to feedback control. In addition, this control scheme can stabilize unstable orbits and is inherently non-invasive.

The phase shift θ is determined with a phase detector (implemented with adaptive filters [17, 29]), and the difference between this phase shift and the target θ_* is fed to a proportional-integral (PI) controller which automatically adjusts the excitation frequency

$$\omega(t) = \omega(0) + \int_0^t k_{i,\theta}(\theta_* - \theta(\tau))d\tau + k_{p,\theta}(\theta_* - \theta(t)) \quad (5)$$

to enforce the desired phase, where $k_{p,\theta}$ and $k_{i,\theta}$ are the proportional and integral gains of the controller, respectively.

Figure 2 represents a block diagram of a PLL testing apparatus. By changing the target θ_*, it is possible to measure the NFRC around a resonance. When considering a primary resonance, the phase shift θ is determined by monitoring the fundamental harmonic response, which is directly excited. Instead, for a generic $m:l$ secondary resonance, the m^{th} harmonic of the response is monitored, as this component resonates with the excitation through the m/l frequency ratio [18]. More details about PLLs are available in [14, 19].

2.2 Broadband data-based modeling: HB-NSI

NSI is adopted in this paper to identify the nonlinear state-space model of the system starting from a broadband measurement. The reader is referred to [7] for a detailed explanation of the method, while a brief overview is reported here.

Let us consider a nonlinear mechanical system described by the following *extended* state-space formulation:

$$\begin{cases} \dot{\boldsymbol{x}}(t) = \boldsymbol{A}\boldsymbol{x}(t) + \boldsymbol{B}^{\mathrm{e}}\boldsymbol{f}^{\mathrm{e}}(\boldsymbol{y},\dot{\boldsymbol{y}},t) \\ \boldsymbol{y}(t) = \boldsymbol{C}\boldsymbol{x}(t) + \boldsymbol{D}^{\mathrm{e}}\boldsymbol{f}^{\mathrm{e}}(\boldsymbol{y},\dot{\boldsymbol{y}},t). \end{cases} \tag{6}$$

where $\boldsymbol{y}(t) \in \mathbb{R}^N$ is the output vector, $\boldsymbol{x} = \left[\boldsymbol{y}^{\mathrm{T}}, \dot{\boldsymbol{y}}^{\mathrm{T}}\right]^{\mathrm{T}}$ is the state vector and $\boldsymbol{f}^{\mathrm{e}}$ is the so-called extended-input vector. This vector stacks the measured input vector $\boldsymbol{f}(t)$ with a collection of J nonlinear basis functions $g_{j=1,\ldots,J} = g_j(\boldsymbol{y},\dot{\boldsymbol{y}},t)$ used to describe the functional behavior of the nonlinearities of the system:

$$\boldsymbol{f}^{\mathrm{e}}(\boldsymbol{y},\dot{\boldsymbol{y}},t) = \left[\boldsymbol{f}(t)^{\mathrm{T}}, -g_1(\boldsymbol{y},\dot{\boldsymbol{y}},t), \ldots, -g_J(\boldsymbol{y},\dot{\boldsymbol{y}},t)\right]^{\mathrm{T}}. \tag{7}$$

These basis functions are assumed to depend on the system displacements and/or velocities and are considered prior knowledge within the framework of NSI. The matrices $\boldsymbol{A}, \boldsymbol{B}^{\mathrm{e}}, \boldsymbol{C}, \boldsymbol{D}^{\mathrm{e}}$ of Eq. (6) are the state, extended input, output and extended direct feedthrough matrices, respectively, and they are identified using subspace identification techniques [9]. It is worth noticing that the matrix $\boldsymbol{A}$ is the state-matrix of the underlying linear system (ULS), thus the underlying-linear dynamics of the structure can be easily estimated by classical eigenvalue decomposition of $\boldsymbol{A}$.

The harmonic balance method can be directly applied to the nonlinear state-space formulation of Eq. (6) by writing it in the frequency domain up to a selected order H, as in [7]:

$$\begin{cases} (\nabla \otimes \boldsymbol{I}_{2N})\boldsymbol{X} = (\boldsymbol{I}_{\tilde{H}} \otimes \boldsymbol{A})X + (\boldsymbol{I}_{\tilde{H}} \otimes \boldsymbol{B}^{\mathrm{e}})\boldsymbol{F}^{\mathrm{e}} \\ \boldsymbol{I}_{N\tilde{H}}\boldsymbol{Y} = (\boldsymbol{I}_{\tilde{H}} \otimes \boldsymbol{C})X + (\boldsymbol{I}_{\tilde{H}} \otimes \boldsymbol{D}^{\mathrm{e}})\boldsymbol{F}^{\mathrm{e}} \end{cases}. \tag{8}$$

Here, $\widetilde{H} = 2H + 1$, $\boldsymbol{I}$ is the identity matrix and $\otimes$ is the Kronecker tensor product. The vectors $\boldsymbol{X}$, $\boldsymbol{Y}$ and $\boldsymbol{F}^{\mathrm{e}}$ contain the Fourier coefficients of the corresponding time vectors $\boldsymbol{x}$, $\boldsymbol{y}$ and $\boldsymbol{f}^{\mathrm{e}}$. Taking the state vector as an example, this yields:

$$\boldsymbol{x}(t) = \boldsymbol{X}^{(0)} + \sum_{h=1}^{H}\left(\boldsymbol{X}_{\mathrm{c}}^{(h)}\cos(h\omega t) + \boldsymbol{X}_{\mathrm{s}}^{(h)}\sin(h\omega t)\right) \tag{9}$$

The operator ∇ in Eq. (8) is defined as:

$$\nabla = \mathrm{diag}(0, \nabla_1, \ldots, \nabla_H), \quad \nabla_h = h\omega\begin{bmatrix} 0 & 1 \\ -1 & 0 \end{bmatrix}. \tag{10}$$

The input–output relation can be obtained by rearranging Eq. (8) as

$$\begin{aligned} \boldsymbol{I}_{N\tilde{H}}\boldsymbol{Y} &= [(\boldsymbol{I}_{\tilde{H}} \otimes \boldsymbol{D}^{\mathrm{e}}) \\ &\quad + (\boldsymbol{I}_{\tilde{H}} \otimes \boldsymbol{C})(\nabla \otimes \boldsymbol{I}_{2N} - \boldsymbol{I}_{\tilde{H}} \otimes \boldsymbol{A})^{-1}(\boldsymbol{I}_{\tilde{H}} \otimes \boldsymbol{B}^{\mathrm{e}})]\boldsymbol{F}^{\mathrm{e}} \\ &= \boldsymbol{\Lambda}^{\mathrm{e}}(\omega)\boldsymbol{F}^{\mathrm{e}}. \end{aligned} \tag{11}$$

The matrix $\boldsymbol{\Lambda}^{\mathrm{e}}(\omega)$ relates the inputs to the outputs and is a function of the identified state-space matrices. As for the vector $\boldsymbol{F}^{\mathrm{e}}$, it contains the Fourier coefficients of both the forcing term and the nonlinear basis functions. The latter depend on displacements and/or velocities, and therefore their Fourier coefficients are a function of $\boldsymbol{Y}$. Since the vector $\boldsymbol{Y}$ is unknown, a recursive methodology must be implemented. This leads to the following nonlinear problem:

$$\boldsymbol{\varepsilon}(\boldsymbol{Y},\omega) = \boldsymbol{\Lambda}^{\mathrm{e}}(\omega)\boldsymbol{F}^{\mathrm{e}}(\boldsymbol{Y}) - \boldsymbol{I}_{N\tilde{H}}\boldsymbol{Y} = 0 \tag{12}$$

which can be solved using an incremental-iterative Newton–Raphson procedure. The quantity $\boldsymbol{F}^{\mathrm{e}}$ can be computed by applying the alternating frequency/time domain

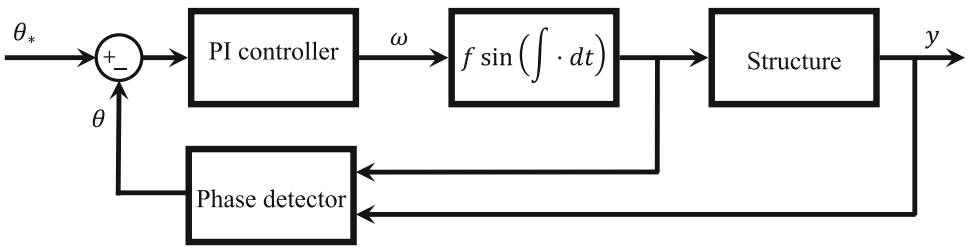

Fig. 2 PLL schematics

technique (AFT) [30], in particular with the formulation described in [7].

Equation (12) can be solved in conjunction with a numerical continuation technique to obtain the nonlinear frequency response curves (NFRCs) of the system and track its bifurcations. In particular, pseudo-arc length continuation [8] is employed in this study. It is important to highlight that the accuracy of the predicted periodic solutions strongly depends on the quality of the identified state-space model. To ensure adequate accuracy, the model should be validated against independent datasets (e.g., via fit percentage or error metrics) and demonstrate consistent predictive performance across the range of excited amplitudes and frequencies [7, 31]. Furthermore, the range of motion of the periodic solutions should be largely within the one covered by the broadband data to avoid extrapolation issues, as outlined in [32, 33].

2.3 Metrics for NFRC comparison

To quantify the agreement between the methods, the normalized mean absolute error (NMAE) is defined as:

$$\varepsilon_h = 100 \frac{E\left[\left|\left|Y_{\text{exp}}^{(h)}\right| - \left|Y_{\text{mod}}^{(h)}\right|\right|\right]}{\max\left|Y_{\text{exp}}^{(h)}\right|}, \tag{13}$$

where $\left|Y_{\text{exp}}^{(h)}\right|$ and $\left|Y_{\text{mod}}^{(h)}\right|$ denote the h-order amplitudes of experimental and modeled curves, respectively, and $E[\cdot]$ is the expectation operator over the considered frequency range. This error, expressed in percentage, provides a scale-independent measure of the overall discrepancy for the harmonic contribution considered, although it is not highly sensitive to local differences. For this reason, the NFRCs will also be represented graphically on logarithmic scales considering the most relevant harmonic contributions.

3 Results: electronic Duffing oscillator

The setup considered in this section is an electronic Duffing oscillator, i.e., a circuit that replicates the dynamics of a Duffing oscillator, whose picture is shown in Fig. 3. It takes a forcing signal as input and outputs signals which are proportional to the velocity and displacement of the oscillator. The parameters of this oscillator can be adjusted with three knobs, that regulate the damping ratio ζ, the natural frequency ω_n and the cubic stiffness coefficient k_3. More details about this circuit are given in [27]. This circuit was connected to a real-time control unit (MicroLabBox from dSPACE) which was programmed to implement either an experimental continuation approach or to generate a broadband excitation signal.

Two scenarios are considered in this paper concerning two different damping ratios (first knob). The other two knobs (natural frequency and nonlinear coefficient) are kept constant. For each scenario, the state-space model of HB-NSI method is estimated from a broadband test in open-loop condition, considering quadratic and cubic nonlinear basis functions of displacements (see Sect. 2.2). The equation of motion of the identified system thus reads:

$$m\ddot{y} + c_v\dot{y} + k_1 y + k_2 y^2 + k_3 y^3 = u(t), \tag{14}$$

where $y(t)$ is the output signal in V, $u(t)$ is the input signal in V, m is the mass, c_v is the viscous damping coefficient, k_1, k_2 and k_3 are the linear, quadratic and cubic coefficients, respectively. It is worth noting that the system is not designed to exhibit quadratic nonlinearity in principle, but the latter is present due to inevitable offsets in the electronics.

3.1 Nonlinear system identification

The nonlinear model is estimated from a broadband test in open-loop condition, lasting for 120 s and sampled at 5000 Hz. The last 20 s of the acquisition are used as a validation set, while the rest is used to estimate the nonlinear state-space model of order 2. The natural frequency and damping ratio of the ULS in the two damping scenarios are listed in Table 1, while the corresponding linear FRFs are shown in Fig. 4.

The estimated coefficients of quadratic and cubic nonlinear terms are listed in Table 2, and show a strong consistency between the two scenarios. It is worth reminding that the coefficients are derived in NSI as the real spectral average of frequency-dependent complex quantities [9]. The standard deviation of these quantities is also reported in Table 2 in brackets, to give an estimate of the variance of the coefficients across the considered frequency range.

As an example, the identified nonlinear restoring force for case 2 is shown in Fig. 5. The cubic nonlinearity is predominant, although a smaller quadratic contribution is visible, accounting for averagely 3% of the nonlinear restoring force on the considered range of motion.

The identified models are validated using the validation set in both scenarios. To this end, the state-space model is

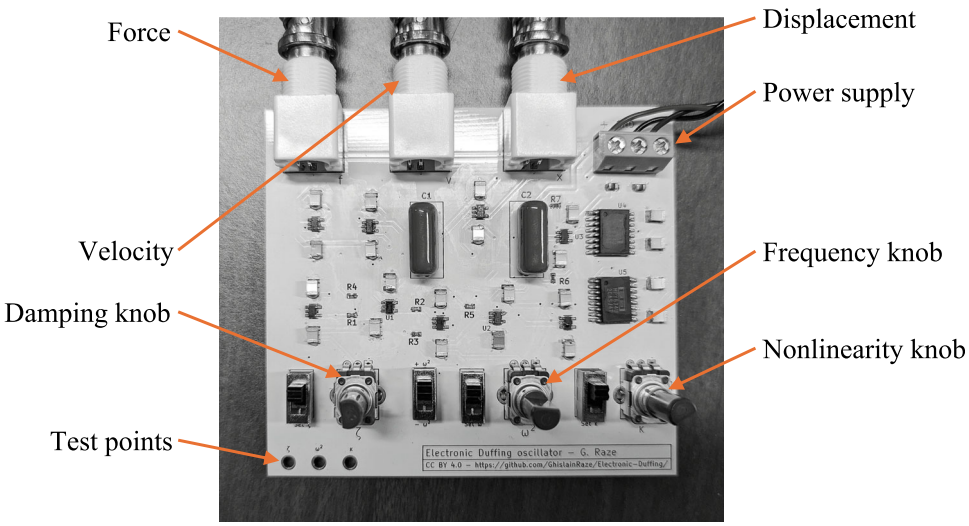

Fig. 3 Electronic Duffing oscillator

Table 1 Parameters of the ULS

	Natural frequency (Hz)	Damping ratio (%)
Case 1 (low damping)	36.94	0.16
Case 2 (medium damping)	36.82	0.74

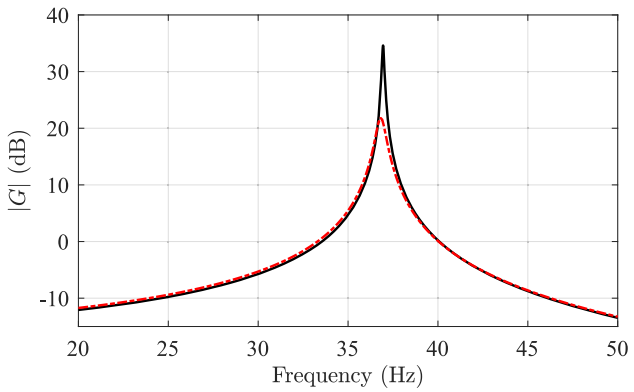

Fig. 4 Frequency response function of the ULS identified with NSI. Black line: case 1, low damping. Dashed-dotted red line: case 2, medium damping

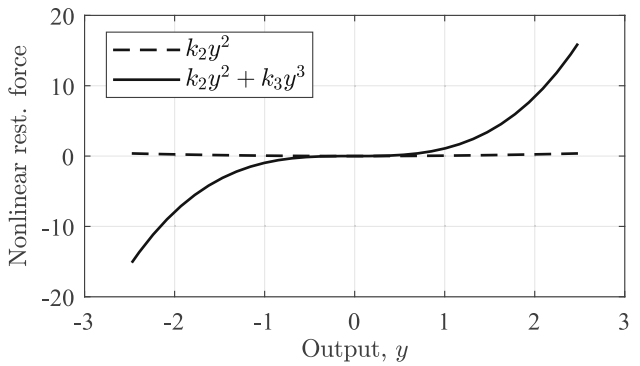

Fig. 5 Nonlinear restoring force estimated with NSI, damping case 2

3.2 Primary resonance

Table 2 Coefficients of the nonlinear terms. Standard deviation is reported in brackets

	Quadratic nonlinearity $[V^{-1}]$	Cubic nonlinearity $[V^{-2}]$
Case 1 (low damping)	0.07 ($2\bullet10^{-5}$)	1.02 ($3\bullet10^{-4}$)
Case 2 (medium damping)	0.06 ($1\bullet10^{-5}$)	1.02 ($3\bullet10^{-4}$)

used to predict the response y_{pred} of the system given the input data from the validation set, u_{val}. Subsequently, y_{pred} is compared with the measured response y_{val}, returning an error of roughly 4% in both cases. The result is visible in Fig. 6.

The comparison between experimental continuation (ACBC) and broadband data-based modeling is initially conducted around the primary resonance of the system, using the state-space model identified in the previous section and with three excitation levels for each damping case. Figure 7, 8 show the amplitudes of the first three harmonics of the system response obtained with experimental continuation and HB-NSI for damping case 1 and 2. Higher

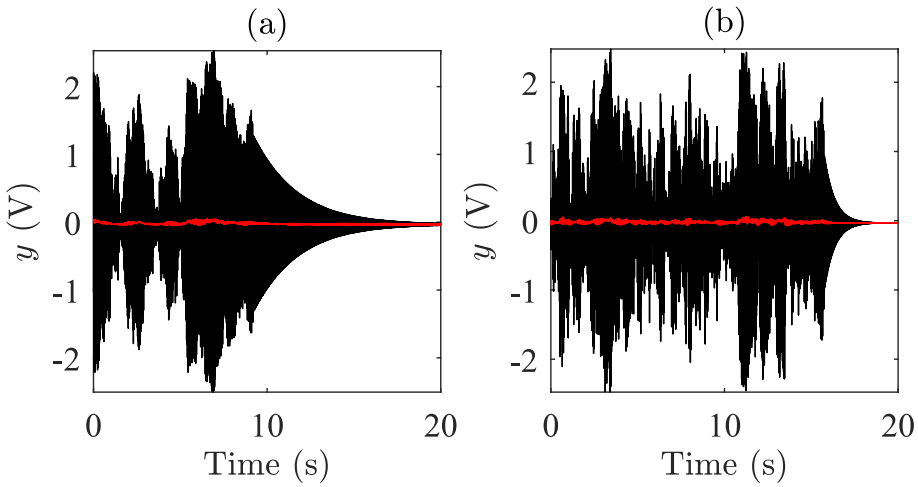

Fig. 6 Validation set. Black line: measured output data (y_{val}). Red line: NSI residual ($y_{val} - y_{pred}$). Damping case 1 in (**a**), damping case 2 in (**b**)

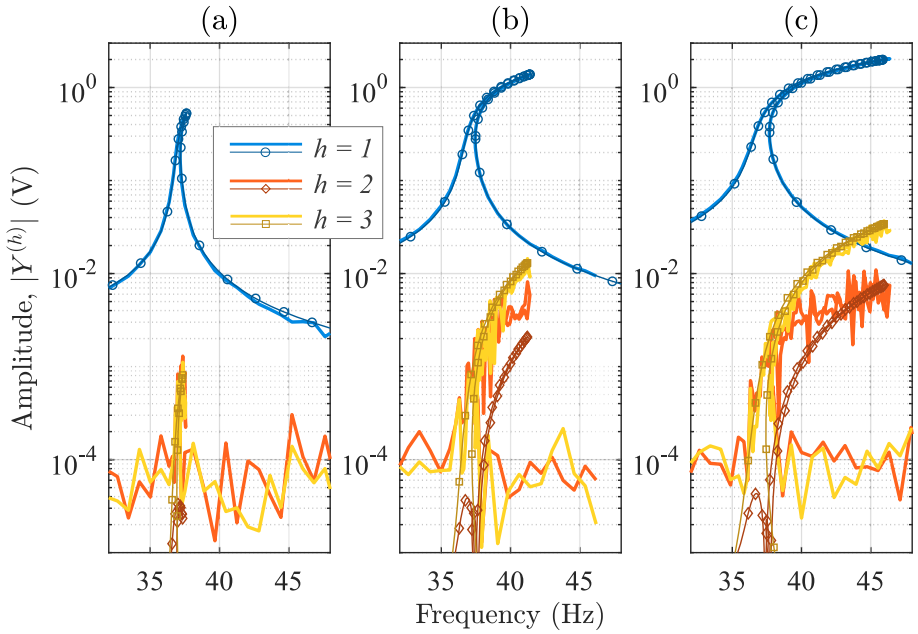

Fig. 7 Primary resonance for three excitation levels, damping case 1. Continuous lines: experimental continuation (ACBC); marked lines: HB-NSI. Input levels: **a** 0.01 V; **b** 0.03 V; **c** 0.05 V

harmonics are negligible and not displayed to ease the reading of the plots. The results from both methods are in strong agreement and primarily dominated by the fundamental harmonic, with an error ε_1 of approximately 7% for both damping levels. The third and second harmonics remain several orders of magnitude below the first and are mostly below the sensitivity level of the voltage sensors in ACBC. This results in noisy signals, which are clearly visible in the continuous lines of Fig. 7 and Fig. 8. Among the two, the third harmonic is more prominent and better captured, as it is linked to the cubic nonlinearity. The third-order NMAE ε_3 is around 11% for the highest excitation level. There is less agreement regarding the second harmonic because it is linked to non-idealities in the circuit that are only partially captured by the quadratic term, yielding an error ε_2 of 22% for the highest excitation. It is worth reminding that both experimental continuation and HB-NSI techniques can compute stable and unstable solutions branches. In this case, unstable solutions are determined by a fold bifurcation, which is typical for this type of system.

3.3 Secondary resonances

The comparison is further extended to examine the system response around secondary resonances in the superharmonic regime, focusing on the 3:1 and 2:1 resonance phenomena.

As anticipated in Sect. 2.1 and shown in [19], ACBC can be inadequate around strong secondary resonances because of the adaptive filters used for the online Fourier decomposition. These filters are designed to isolate the

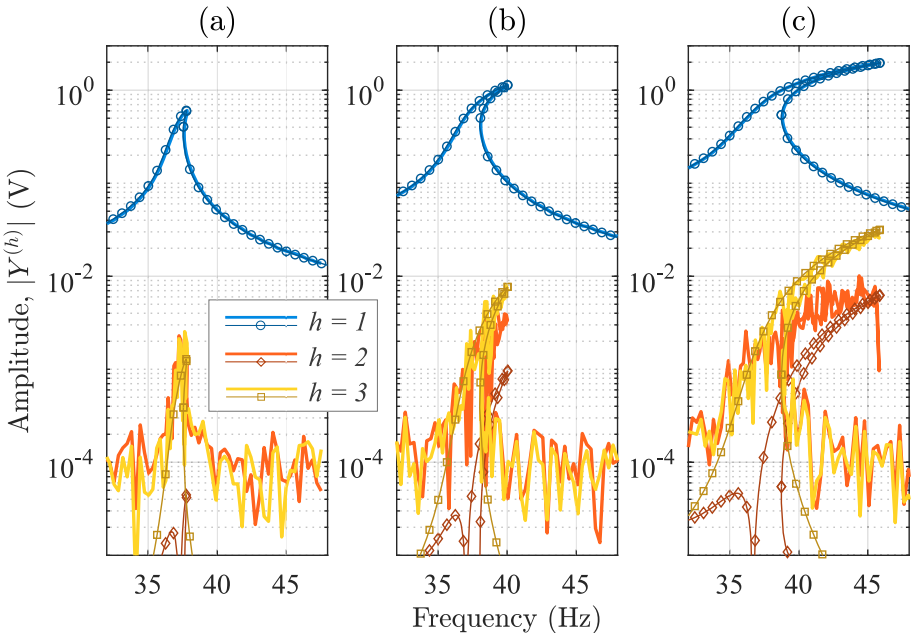

Fig. 8 Primary resonance for three excitation levels, damping case 2. Continuous lines: experimental continuation (ACBC); marked lines: HB-NSI. Input levels: **a** 0.05 V; **b** 0.10 V; **c** 0.20 V

fundamental harmonic of the response, thereby allowing the controller to enforce the desired amplitude-frequency condition without interfering with the underlying system dynamics. However, near strong superharmonic resonances, adaptive filters fail in separating these components in real time due to the significant contributions from higher-order harmonics. As a consequence, the control input acquires residual harmonic contents, which interact dynamically with the system and violate the non-invasiveness condition. This issue can be inspected by checking the harmonic components of $y_*(t) - y(t)$ (refer to Eq. (2)). For the control to remain non-invasive, this quantity must exhibit a mono-harmonic nature. Figure 9 illustrates the first five harmonics of this quantity in two scenarios: (a) around one primary resonance, and (b) around one secondary resonance. In scenario (a), the first harmonic remains approximately constant, while higher harmonics are effectively negligible. Conversely, in scenario (b), the third harmonic becomes significant in the vicinity of the 3:1 resonance region. For these reasons, ACBC will not be used for secondary resonances. In contrast, PLL has proved robust in characterizing these responses [18, 34] and is therefore adopted for this analysis.

The results are thoroughly examined in Fig. 10, 11, which show the first three harmonic components of the response under low (case 1) and medium (case 2) damping conditions. Higher harmonics are not displayed to ease the reading of the plots. In both cases, the results from experimental continuation (PLL) and the HB-NSI method are found to be highly similar, with particularly close

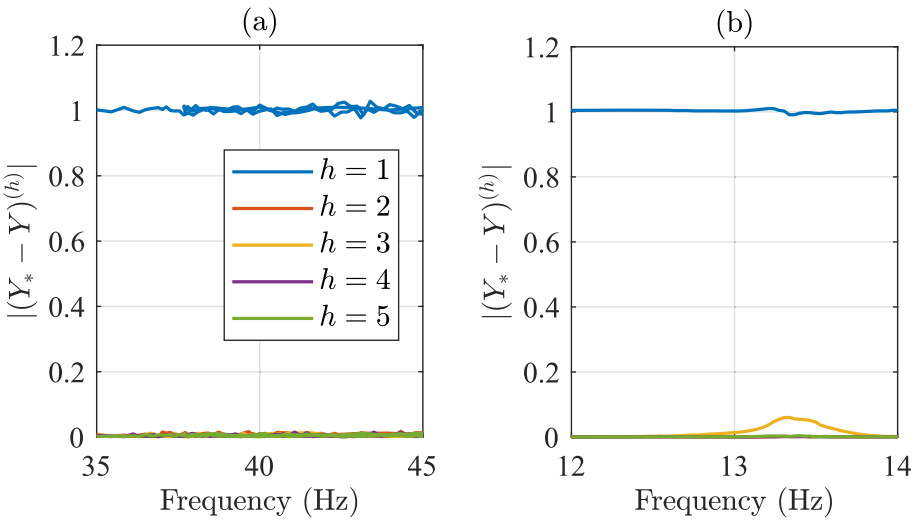

Fig. 9 Invasiveness of control in ACBC. Primary resonance case in (**a**), secondary resonance case in (**b**)

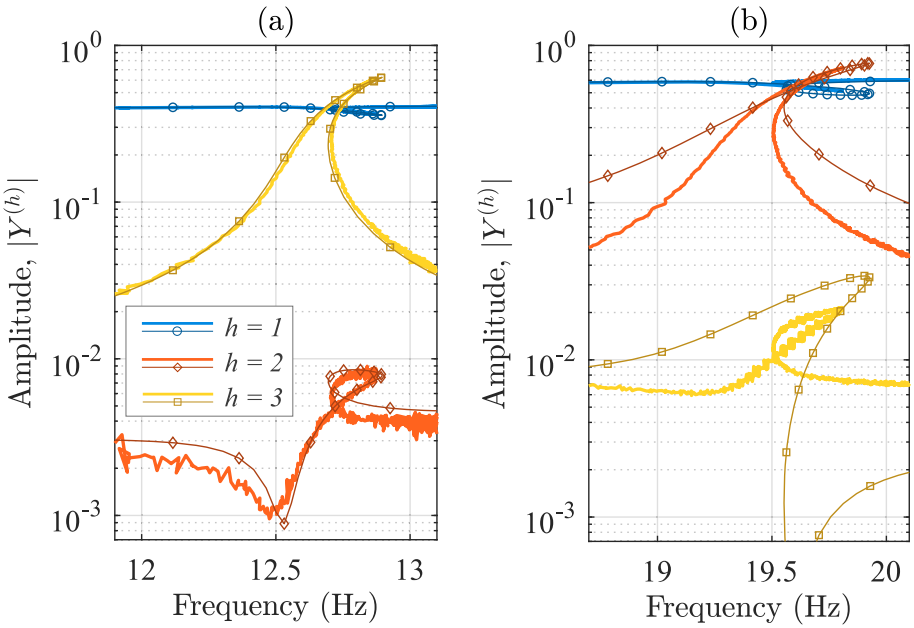

Fig. 10 Secondary resonance, damping case 1. Continuous lines: experimental continuation (PLL); marked lines: HB-NSI. 3:1 resonance in (**a**), 2 V input level; 2:1 resonance in (**b**), 2 V input level

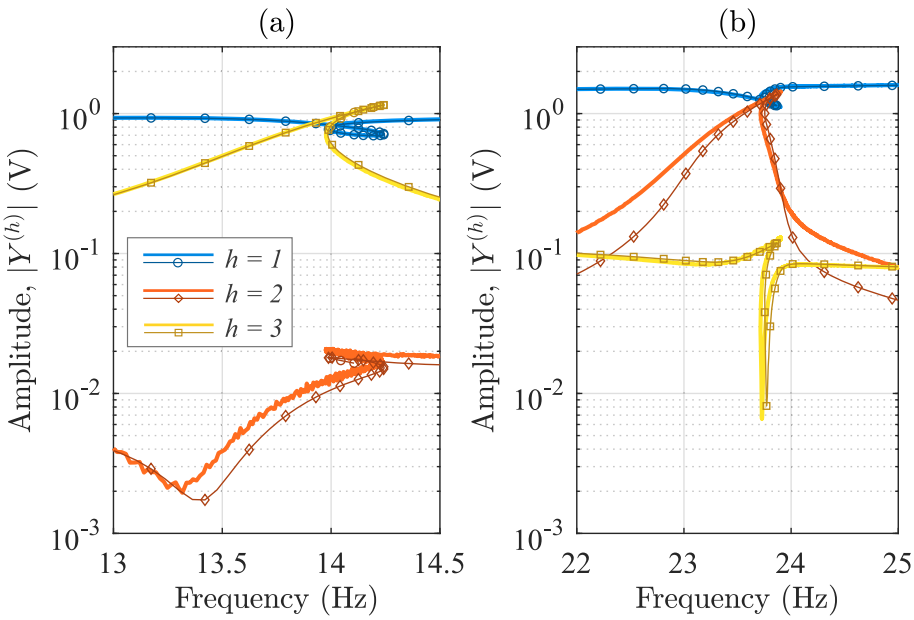

Fig. 11 Secondary resonance, damping case 2. Continuous lines: experimental continuation (PLL); marked lines: HB-NSI. 3:1 resonance in (**a**), 5 V input level; 2:1 resonance in (**b**), 8 V input level

matching in the medium damping case. Here, the average fundamental NMAE is 2%, compared to 12% for the low-damped case.

In the 3:1 case, the response is primarily influenced by the first and third harmonics, as expected. In the low-damped scenario (Fig. 10a), there is a solid agreement between the two approaches, with minor discrepancies observed in the even harmonics, which exhibit low amplitudes and hence have a negligible effect on the overall response. In the medium-damped case (Fig. 11a), both methods align almost perfectly, confirming the robustness and accuracy of both approaches under these conditions.

The 2:1 resonance case presents a greater challenge, primarily due to the weak quadratic nonlinearity. As a result, the response is predominantly influenced by the first and second harmonics. This causes the two methods to diverge more significantly, especially in the low-damped scenario (Fig. 10b). In this case, the overall behavior of the single harmonic contributions is similar between the two

approaches, but visible differences exist. Damping case 2 (Fig. 11b) shows notably superior results, with consistent agreement between the two methods across all the harmonic contributions.

4 Results:thin-walled nonlinear beam

To further substantiate the comparison made in this work with a more challenging example, a stainless steel clamped–clamped beam of dimensions 750 mm × 20 mm × 2 mm similar to that considered in [34] is now studied. It is excited with a current-driven electrodynamic shaker and endowed with seven accelerometers distributed along its span to monitor its response. The signals of the accelerometers were recorded by a Scadas Mobile unit from Siemens. The shaker was either driven by the same unit for broadband tests, or by a MicroLabBox for experimental continuation tests. Figure 12 shows a picture of the setup.

Broadband tests were realized for NSI with an excitation bandwidth from 5 to 150 Hz, encompassing the first four vibration modes, and a sampling frequency of 6400 Hz. The NFRCs identified using HB-NSI are then compared to those obtained by ACBC. The 3:1 and 2:1 superharmonic resonances of the first mode of the beam were also measured using PLL. Because this is a flexible structure, collocated control is virtually mandatory to avoid closed-loop instabilities [35]. The feedback signal used by ACBC was the lowpass-filtered voltage across the electrodes of the shaker to minimize that risk. Intuitively, using the current and voltage as collocated input and output ensures that the power injected into or extracted from the system is mastered, and instabilities are thus avoided. By contrast, PLL does not have such collocation requirements because it adjusts the forcing frequency instead of the forcing signal itself. The feedback signal used for PLL was thus the acceleration at the middle of the beam, because the mode of interest (mode 1) is much more responsive therein. For more details about these aspects, we refer to [19].

4.1 Nonlinear system identification

Geometrical nonlinearity arises in the considered structure when undergoing large-amplitude vibrations [1]. This results in a distributed nonlinear strain–displacement relation coupling bending and in-plane stretching deformations. Given the distributed nature of the nonlinearity in this case, the nonlinear state-space model is identified in a reduced-order domain using the methodology presented in [36]. The linear normal modes (LNMs) ϕ of the system are initially obtained from a low-level random test, and used as projection basis for the high-level nonlinear test, as commonly done in these kind of systems [37–39]. The physical displacements $y(x,t)$ are therefore written as:

$$y(x,t) \cong \sum_{r=1}^{N} \phi_r(x)\gamma_r(t), \tag{15}$$

with $\gamma_r(t)$ the r^{th} modal coordinate. The term *modal* here is adopted in relation to the reduced-order domain, although LNMs do not decouple the equation of motions in a nonlinear setting. The r^{th} equation of motion in the reduced-order domain can be written as [36, 39]:

$$m_r\ddot{\gamma}_r + c_r\dot{\gamma}_r + k_r\gamma_r + \sum_{i=1}^{N}\sum_{j\geq i}^{N} {}_r\alpha_{ij}\gamma_i\gamma_j + \sum_{i=1}^{N}\sum_{j\geq i}^{N}\sum_{k\geq j}^{N} {}_r\beta_{ijk}\gamma_i\gamma_j\gamma_k = q_r, \tag{16}$$

where m_r, c_r and k_r are the mass, viscous damping and stiffness terms, ${}_r\alpha_{ij}$ and ${}_r\beta_{ijk}$ are the coefficients of the nonlinear functions, and q_r is the external forcing term. The nonlinear basis functions contain quadratic and cubic combinations of the modal coordinates of the considered modes. With four modes in the excitation frequency range, this results in a total of 30 nonlinear terms.

Figure 13 shows histograms of the measured displacements for both low-level and high-level multisine random tests, illustrating the considered range of motion. The displacement values have been obtained by double integration of the acceleration signals using a Kalman filter followed by a high-pass Butterworth filter to remove low-frequency drift (below 5 Hz).

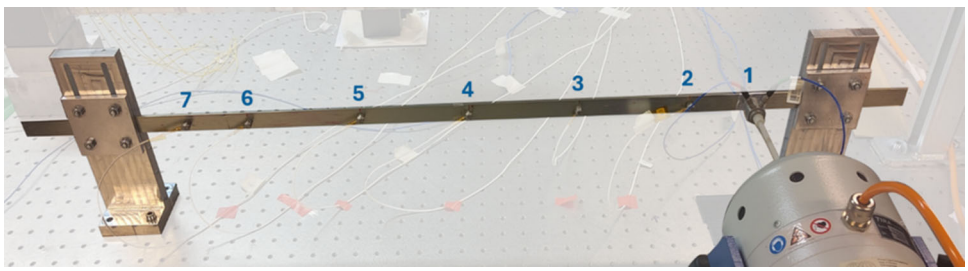

Fig. 12 Picture of the nonlinear beam

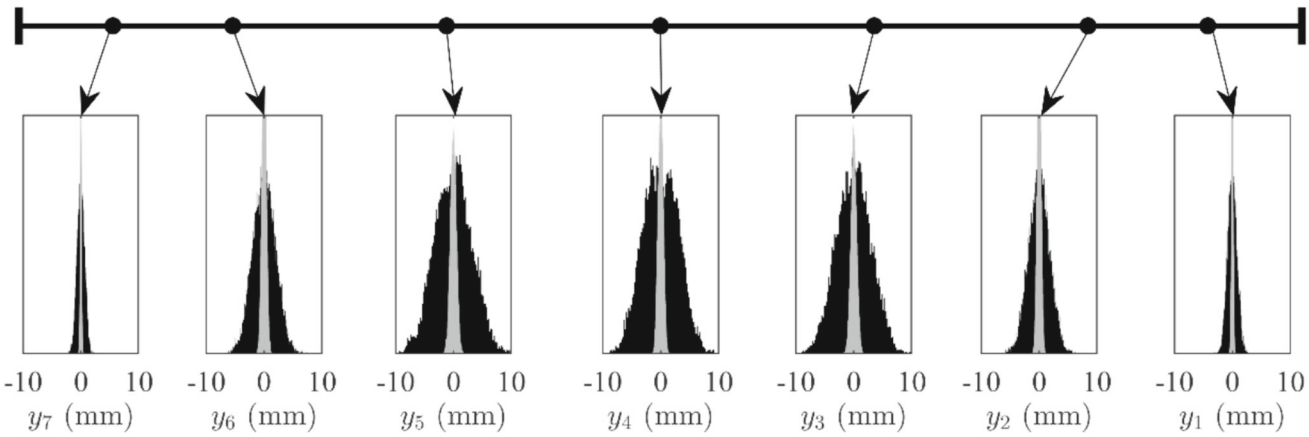

Fig. 13 Histograms of measured displacements, random tests. Gray: low excitation level; black: high excitation level

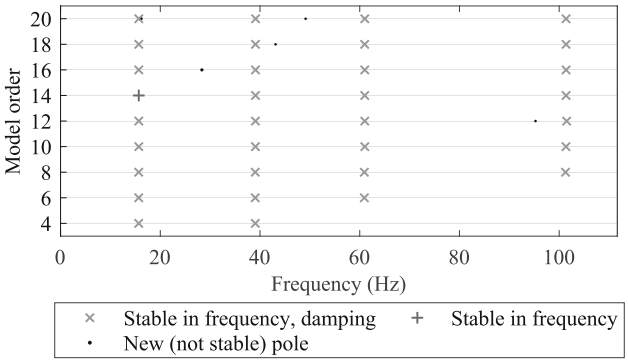

Fig. 14 Stabilization diagram of the ULS. Stabilization thresholds for natural frequency and damping ratio are 0.5% and 10%, respectively

Table 3 Modal parameters of the ULS

Mode nr	Natural frequency (Hz)		Damping ratio (%)	
	NSI (ULS)	Low-level	NSI (ULS)	Low-level
1	15.67	15.90	1.41	1.56
2	39.04	39.39	1.42	1.51
3	60.93	61.25	1.36	1.20
4	101.27	101.52	0.93	0.98

The stabilization diagram of the ULS obtained applying NSI is displayed in Fig. 14, and a model order equal to 8 is selected. The modal parameters of the ULS are listed in Table 3, and compared to the ones retrieved from the low-level (linear) test using linear subspace identification (SI). The FRFs of the ULS for sensors 3 and 6 are presented in Fig. 15 and compared to the low-level ones. Results are displayed in physical coordinates, obtained by inverse transformation of the modal coordinates through LNMs.

The identified nonlinear model is eventually validated using the last 30 s of data as validation set. The average percentage deviation between predicted and measured outputs across all the sensors is 9%. The result is visible in Fig. 16 for sensors 1 and 5, with similar behavior observed for the other outputs.

4.2 Primary resonances

The identified state-space model is used to generate the NFRCs of the system encompassing the first four modes and considering 9 harmonics. Results are compared to those obtained via ACBC for two excitation levels.

Prior to this step, the range of motion covered by experimental continuation is inspected and compared to the random data used in NSI. The result of this analysis is depicted in Fig. 17 considering modal coordinates, and shows that the highest level of ACBC (0.08 V) visibly exceeds the range of motion used to train the nonlinear state-space model for the first modal coordinate. This implies that extrapolation occurs when generating the corresponding NFRC with HB-NSI, potentially leading to unreliable results. This issue will be further addressed in the subsequent sections, and the reader can refer to [32] for a more in-depth discussion.

It is also important to highlight that the highest level of ACBC required specific adjustments of the control parameters, since the first resonance was difficult to stabilize and required a high differential gain. This, combined with a high cut-off frequency for the lowpass filter, created instabilities at high frequencies. Since higher modes presented fewer challenges, the test was conducted in two phases: initially, a low cut-off frequency and high differential gain were employed to stabilize the first resonance; subsequently, lower gains were applied to fine-tune the controller for higher modes. As of today, there is no automated method for tuning the controller in experimental

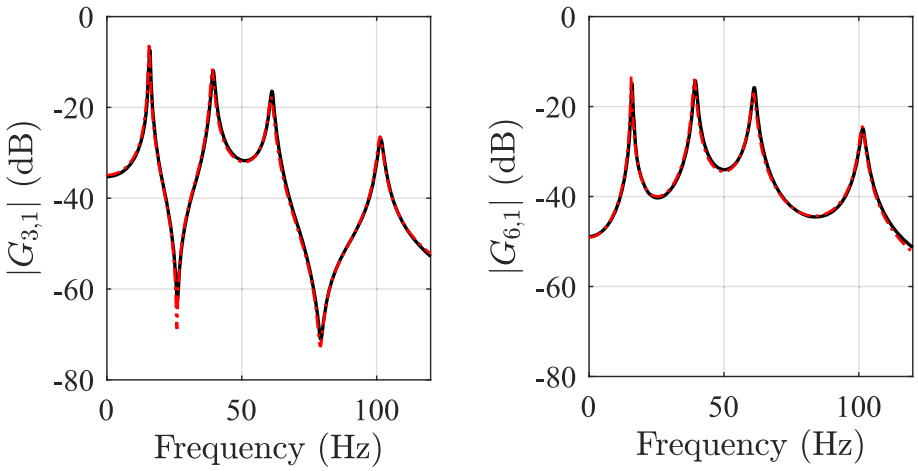

Fig. 15 Linear FRFs. Black line: SI, low-level. Dashed-dotted red line: NSI, ULS

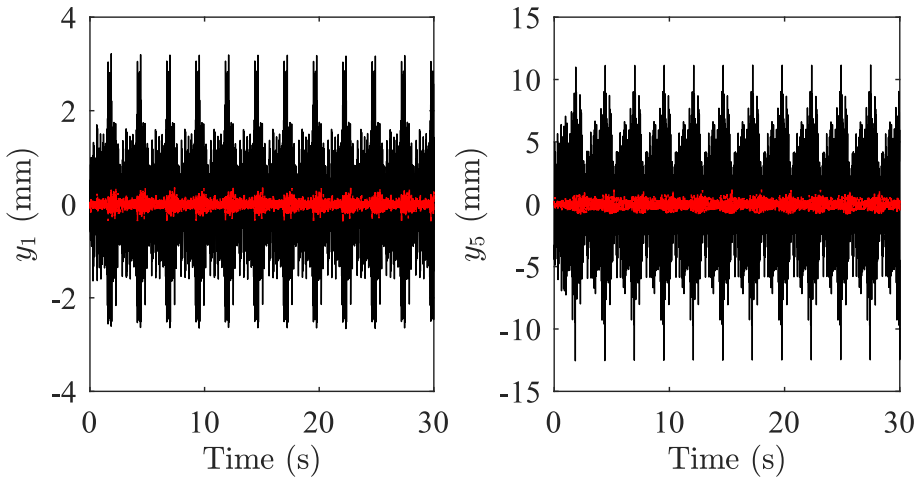

Fig. 16 Validation set. Black line: measured outputs 1 and 5. Red line: NSI residual

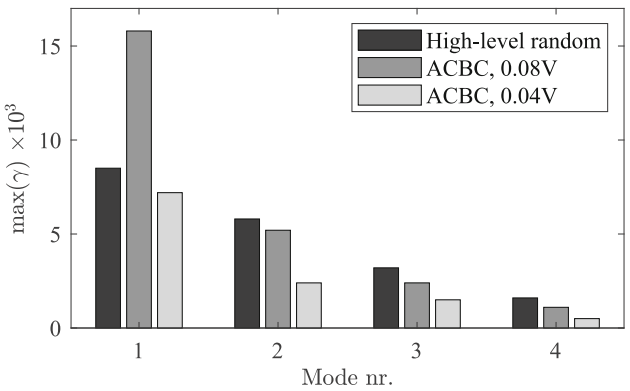

Fig. 17 Range of motion of the modal coordinates for random and ACBC data

continuation techniques to ensure non-invasiveness. The reader is referred to [19] for more details.

The NFRCs of the first four modal coordinates (first harmonic) are displayed in Fig. 18, 19 for the two excitation levels, 0.04 V and 0.08 V, respectively. Results are consistent between the two approaches, particularly at the lowest excitation level. Instead, some discrepancies are observed near the first resonance for the 0.08 V test. In this case, the HB-NSI method extrapolates from the data, making its results uncertain. This highlights the need for sufficient data coverage to ensure model accuracy. However, meeting this requirement might be problematic in tests where nonlinearity must be triggered across multiple modes simultaneously, since sensors might easily saturate.

Figure 20 illustrates the first three harmonic components around the first resonance for the two excitation levels. Second and third harmonics are weakly present in both cases, with similar peak values for both methods. Higher harmonics are negligible, and not displayed to ease the reading of the plots.

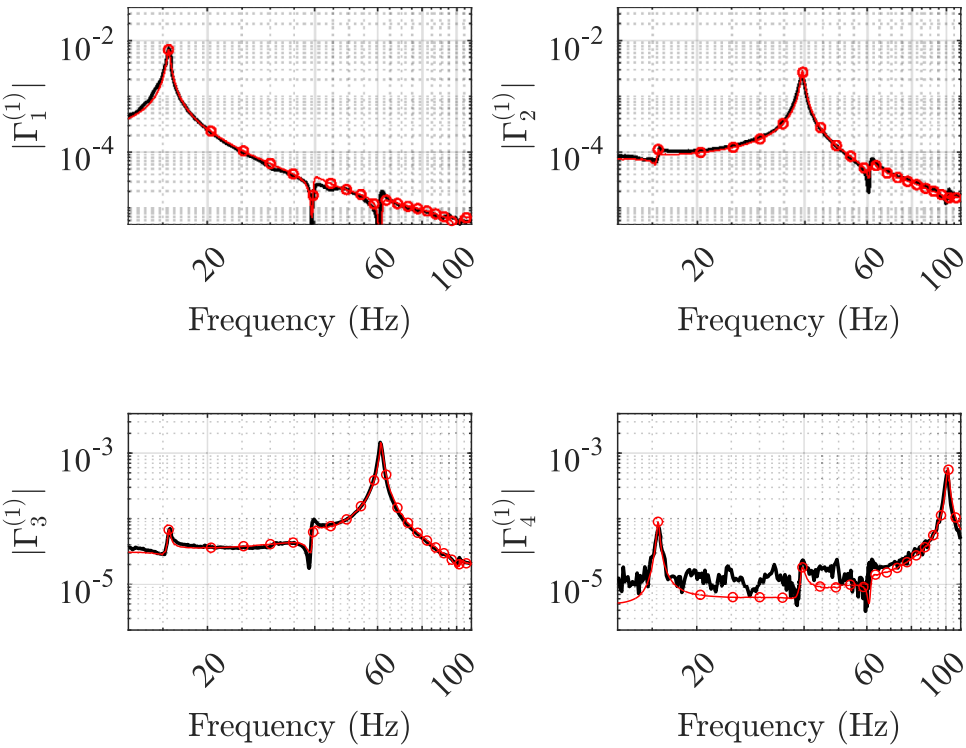

Fig. 18 Primary resonances of the nonlinear beam, 0.04 V input level. Continuous black line: experimental continuation (ACBC); marked red line: HB-NSI

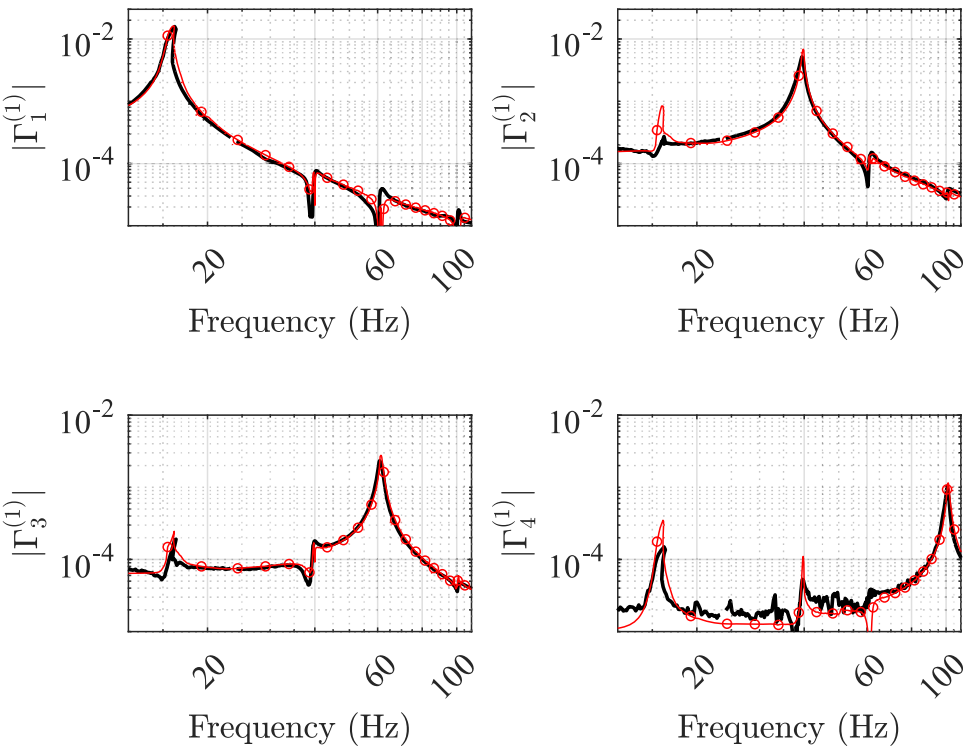

Fig. 19 Primary resonances of the nonlinear beam, 0.08 V input level. Continuous black line: experimental continuation (ACBC); marked red line: HB-NSI

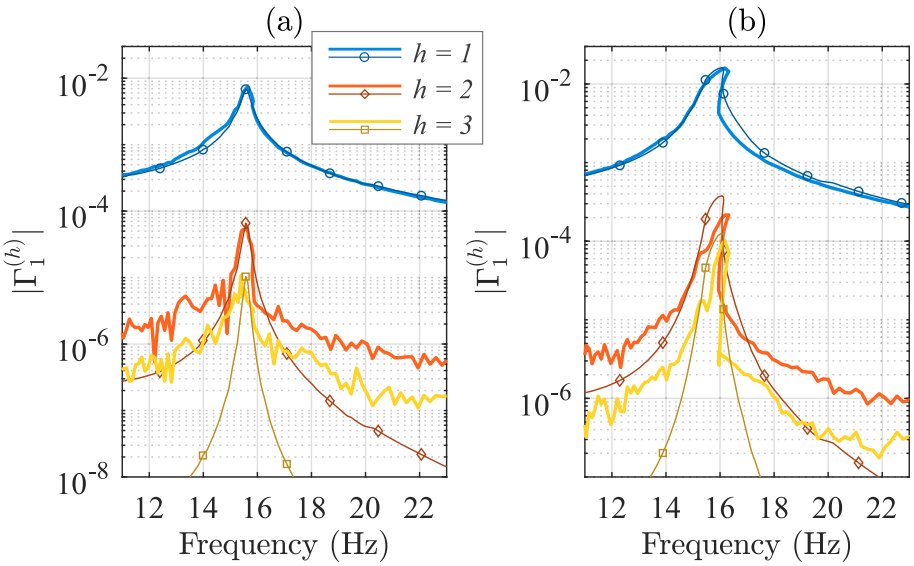

Fig. 20 First primary resonance of the nonlinear beam, harmonic contributions. Continuous lines: experimental continuation (ACBC); marked lines: HB-NSI. Input levels: **a** 0.04 V; **b** 0.08 V

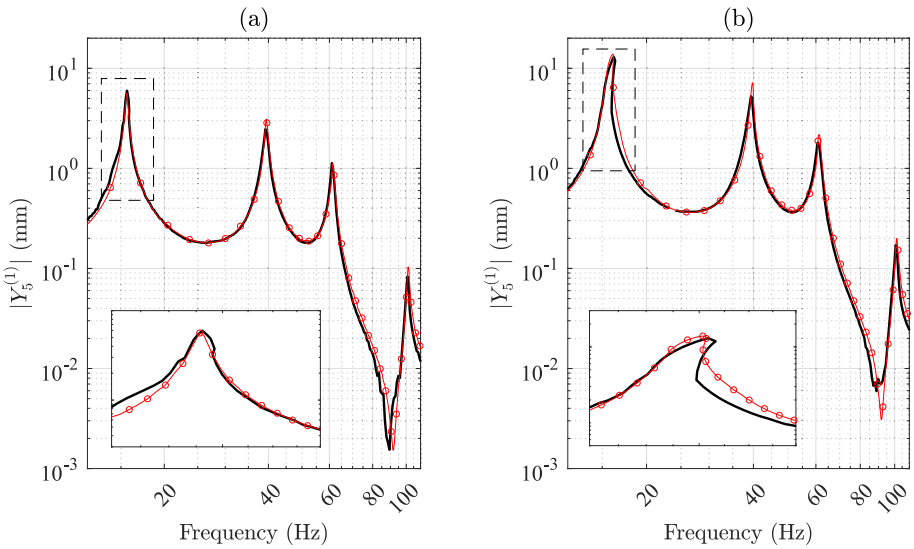

Fig. 21 Primary resonances of the nonlinear beam, sensor 5. Input levels: **a** 0.08 V; **b** 0.04 V. Continuous line: experimental continuation (ACBC); marked red line: HB-NSI. Boxes display a zoom around first resonance

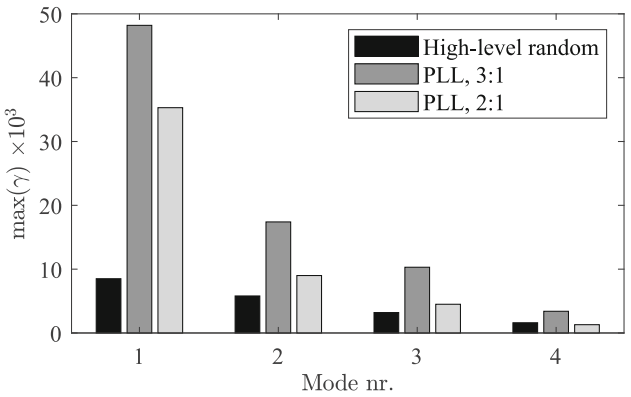

Fig. 22 Range of motion of the modal coordinates for random and PLL data

Eventually, results in the physical domain can be obtained by transforming back the reduced-order coordinates through the LNMs. This is illustrated in Fig. 21 for the two excitation levels considering sensor 5 as an example; the other sensors exhibit similar behavior. The average error ε_1 across all sensors is 5% for the highest excitation level.

4.3 Secondary resonances

Superharmonic resonances 3:1 and 2:1 are investigated in this section. Experimental continuation was performed using PLL for the reasons described in Sect. 2.1. The nonlinear state-space model identified in Sect. 4.1 can be employed in principle to generate the NFRCs within superharmonic frequency ranges, similarly to the case of

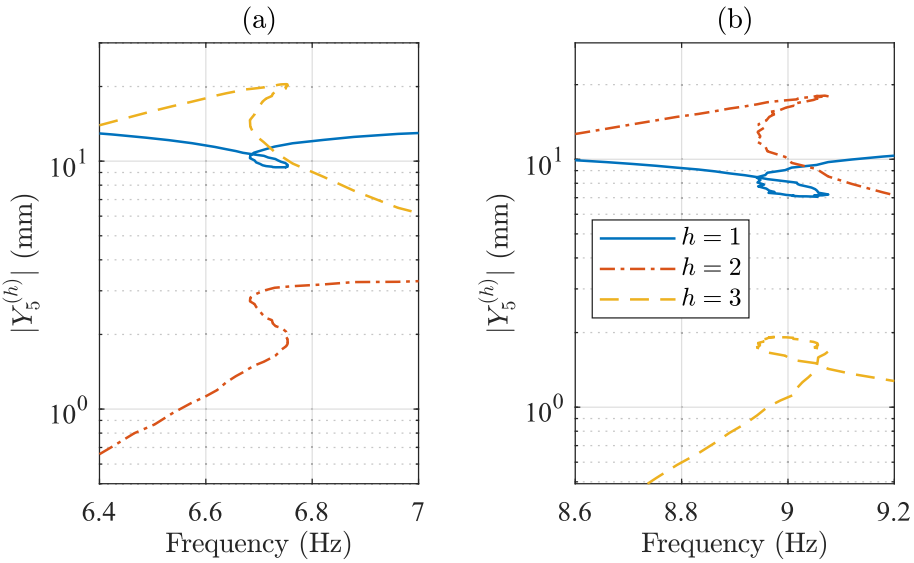

Fig. 23 Secondary resonances of the nonlinear beam, PLL, harmonic contributions. 3:1 resonance in (**a**), 3 V input level; 2:1 resonance in (**b**), 1.5 V input level

Table 4 Summary of the methods

	Broadband data-based modeling	Experimental continuation
Test condition	Open loop	Closed loop (control-based)
Prior information needed	Yes	No
Identification of a mathematical model	Yes (Verify data quality and successful model validation)	No
NFRCs, primary resonances	Yes (Avoid extrapolation)	Yes (Verify data quality, controller tuning and non-invasiveness)
NFRCs, secondary resonances	Yes (Avoid extrapolation)	ACBC: No PLL: Yes (Verify data quality, controller tuning and non-invasiveness)

the electronic Duffing oscillator. However, achieving these resonances requires significantly higher input levels compared to previous measurements in this case, as shown in Fig. 22. At this level of extrapolation, HB-NSI model fails to converge when performing numerical continuation in the selected frequency range, since the nonlinear model becomes unstable. Dedicated random testing would therefore be necessary to accurately identify the nonlinear model within this range of motion.

For the above-mentioned reasons, only PLL results are discussed in this case. Driving voltage values are 3 V for 3:1 case and 1.5 V for 2:1 case. These voltage values were found from preliminary open-loop swept-sine tests in the expected vicinity of the resonance (near $1/m$ times the linear resonance frequency of the first mode). Suitable proportional and integral gains for the controller were then found by trial and error. Figure 23a illustrates the first three harmonic components of 3:1 superharmonic resonance for sensor 5. As expected, the third harmonic resonates and dominates the response, while the first harmonic exhibits a loop. Similarly, Fig. 23b shows the 2:1 superharmonic resonance for the same sensor, where the second harmonic resonates.

5 Conclusions

This paper demonstrates that both experimental continuation and broadband data-based modeling effectively capture the nonlinear resonance behaviors of the system across

primary and secondary resonances, provided that the specific methodological requirements are satisfied. When these conditions are satisfied, the two approaches align well in representing the response of the systems considered in this study. However, if the requirements of either methodology are not adequately fulfilled, the results may diverge and become unreliable. For broadband data-based modeling, this typically occurs due to extrapolation issues or inaccuracies in nonlinear modeling. For control-based continuation, discrepancies are primarily caused by inappropriate tuning of control parameters or invasiveness of the controller, such as in the case of secondary resonances with ACBC. The above considerations are summarized in Table 4. Overall, the study highlights the complementary strengths and limitations of the two classes of approaches and underscores the importance of carefully following methodological requirements. In particular, the analysis of secondary resonances provides a challenging and meaningful benchmark, offering new insights into the robustness and applicability of each method in nonlinear system identification.

Acknowledgements Ghislain Raze is a Postdoctoral Researcher of the Fonds de la Recherche Scientifique—FNRS which is gratefully acknowledged.

Author Contribution D.A.: literature search, methodology, experimental acquisitions, data analysis, investigation, and writing—original and revised draft preparation. G.R.: literature search, methodology, experimental acquisitions, and writing—original and revised draft preparation. S.M.: supervision, and writing—review and editing. G.K.: funding acquisition, supervision, and writing—review and editing.

Funding Open access funding provided by Politecnico di Torino within the CRUI-CARE Agreement. The authors have not disclosed any funding.

Data availability The datasets generated during and/or analysed during the current study are not publicly available but are available from the corresponding author on reasonable request.

Declarations

Conflict of interest The authors declare no competing interests.

References

1. Nayfeh, A.H., Mook, D.T.: Nonlinear Oscillations. Wiley (1995)
2. Gatti, G., Brennan, M.J., Tang, B.: Some diverse examples of exploiting the beneficial effects of geometric stiffness nonlinearity. Mech. Syst. Signal Process. **125**, 4–20 (2019). https://doi.org/10.1016/j.ymssp.2018.08.024
3. Kerschen, G., Worden, K., Vakakis, A.F., Golinval, J.-C.: Past, present and future of nonlinear system identification in structural dynamics. Mech. Syst. Signal Process. **20**, 505–592 (2006). https://doi.org/10.1016/j.ymssp.2005.04.008
4. Noël, J.P., Kerschen, G.: Nonlinear system identification in structural dynamics: 10 more years of progress. Mech. Syst. Signal Process. **83**, 2–35 (2017). https://doi.org/10.1016/j.ymssp.2016.07.020
5. Worden, K., Tomlinson, G.R.: Nonlinearity in structural dynamics: detection, identification, and modelling. Institute of Physics (2001)
6. Noël, J.P., Renson, L., Grappasonni, C., Kerschen, G.: Identification of nonlinear normal modes of engineering structures under broadband forcing. Mech. Syst. Signal Process. **74**, 95–110 (2016). https://doi.org/10.1016/j.ymssp.2015.04.016
7. Anastasio, D., Marchesiello, S.: Nonlinear frequency response curves estimation and stability analysis of randomly excited systems in the subspace framework. Nonlinear Dyn. (2023). https://doi.org/10.1007/s11071-023-08280-6
8. Groll, G.V., Ewins, D.J.: The harmonic balance method with arc-length continuation in rotor/stator contact problems. J. Sound Vib. **241**, 223–233 (2001). https://doi.org/10.1006/jsvi.2000.3298
9. Marchesiello, S., Garibaldi, L.: A time domain approach for identifying nonlinear vibrating structures by subspace methods. Mech. Syst. Signal Process. **22**, 81–101 (2008). https://doi.org/10.1016/j.ymssp.2007.04.002
10. Detroux, T., Renson, L., Masset, L., Kerschen, G.: The harmonic balance method for bifurcation analysis of large-scale nonlinear mechanical systems. Comput. Methods Appl. Mech. Eng. **296**, 18–38 (2015). https://doi.org/10.1016/j.cma.2015.07.017
11. Anastasio, D., Marchesiello, S., Kerschen, G.: Estimation of the periodic solutions of geometrically nonlinear structures by broadband excitation. Presented at the Proceedings of ISMA 2024 - International Conference on Noise and Vibration Engineering and USD 2024 - International Conference on Uncertainty in Structural Dynamics (2024)
12. Sieber, J., Krauskopf, B.: Control based bifurcation analysis for experiments. Nonlinear Dyn. **51**, 365–377 (2008). https://doi.org/10.1007/s11071-007-9217-2
13. Barton, D.A.W., Sieber, J.: Systematic experimental exploration of bifurcations with noninvasive control. Phys. Rev. E **87**, 052916 (2013). https://doi.org/10.1103/PhysRevE.87.052916
14. Peter, S., Leine, R.I.: Excitation power quantities in phase resonance testing of nonlinear systems with phase-locked-loop excitation. Mech. Syst. Signal Process. **96**, 139–158 (2017). https://doi.org/10.1016/j.ymssp.2017.04.011
15. Karaağaçlı, T., Özgüven, H.N.: Experimental modal analysis of nonlinear systems by using response-controlled stepped-sine testing. Mech. Syst. Signal Process. (2021). https://doi.org/10.1016/j.ymssp.2020.107023
16. Renson, L., Gonzalez-Buelga, A., Barton, D.A.W., Neild, S.A.: Robust identification of backbone curves using control-based continuation. J. Sound Vib. **367**, 145–158 (2016). https://doi.org/10.1016/j.jsv.2015.12.035
17. Abeloos, G., Renson, L., Collette, C., Kerschen, G.: Stepped and swept control-based continuation using adaptive filtering. Nonlinear Dyn. **104**, 3793–3808 (2021). https://doi.org/10.1007/s11071-021-06506-z

18. Abeloos, G.: Control-based methods for the identification of nonlinear structures. PhD Thesis, University of Liège (2022)
19. Raze, G., Abeloos, G., Kerschen, G.: Experimental continuation in nonlinear dynamics: recent advances and future challenges. Nonlinear Dyn. (2025). https://doi.org/10.1007/s11071-024-10543-9
20. Beregi, S., Barton, D.A.W., Rezgui, D., Neild, S.A.: Robustness of nonlinear parameter identification in the presence of process noise using control-based continuation. Nonlinear Dyn. **104**, 885–900 (2021). https://doi.org/10.1007/s11071-021-06347-w
21. Mélot, A., Denimal Goy, E., Renson, L.: Nonlinear system identification with control-based continuation of bifurcation curves. In: ENOC 2024 - 11th European Nonlinear Dynamics Conference. pp. 1–2. , Delft, Netherlands (2024)
22. Balaji, N.N., Lian, S., Scheel, M., Brake, M.R.W., Tiso, P., Noël, J.-P., Krack, M.: Numerical assessment of polynomial nonlinear state-space and nonlinear-mode models for near-resonant vibrations. Vibration **3**, 320–342 (2020). https://doi.org/10.3390/vibration3030022
23. Scheel, M., Kleyman, G., Tatar, A., Brake, M.R.W., Peter, S., Noël, J.-P., Allen, M.S., Krack, M.: Experimental assessment of polynomial nonlinear state-space and nonlinear-mode models for near-resonant vibrations. Mech. Syst. Signal Process. **143**, 106796 (2020). https://doi.org/10.1016/j.ymssp.2020.106796
24. Paduart, J., Lauwers, L., Swevers, J., Smolders, K., Schoukens, J., Pintelon, R.: Identification of nonlinear systems using polynomial nonlinear state space models. Automatica **46**, 647–656 (2010). https://doi.org/10.1016/j.automatica.2010.01.001
25. Scheel, M., Peter, S., Leine, R.I., Krack, M.: A phase resonance approach for modal testing of structures with nonlinear dissipation. J. Sound Vib. **435**, 56–73 (2018). https://doi.org/10.1016/j.jsv.2018.07.010
26. Kovacic, I., Brennan, M.J., Michael, J.: The Duffing equation: nonlinear oscillators and their phenomena. Wiley (2011)
27. Raze, G.: An electronic Duffing oscillator, https://github.com/GhislainRaze/Electronic-Duffing
28. Mojrzisch, S., Wallaschek, J., Bremer, J.: An experimental method for the phase controlled frequency response measurement of nonlinear vibration systems. Proc Appl Math and Mech. **12**, 253–254 (2012). https://doi.org/10.1002/pamm.201210117
29. Hippold, P., Scheel, M., Renson, L., Krack, M.: Robust and fast backbone tracking via phase-locked loops. Mech. Syst. Signal Process. **220**, 111670 (2024). https://doi.org/10.1016/j.ymssp.2024.111670
30. Cameron, T.M., Griffin, J.H.: An alternating frequency/time domain method for calculating the steady-state response of nonlinear dynamic systems. J. Appl. Mech. **56**, 149–154 (1989). https://doi.org/10.1115/1.3176036
31. Ljung, L.: Perspectives on system identification. In: Annual Reviews in Control. pp. 1–12. Elsevier Ltd (2010)
32. Anastasio, D., Marchesiello, S., Gatti, G., Gonçalves, P.J.P., Shaw, A.D., Brennan, M.J.: An investigation into model extrapolation and stability in the system identification of a nonlinear structure. Nonlinear Dyn. **111**, 17653–17665 (2023). https://doi.org/10.1007/s11071-023-08770-7
33. Schüssler, M., Nelles, O.: Extrapolation behavior comparison of nonlinear state space models. IFAC-PapersOnLine. **54**, 487–492 (2021). https://doi.org/10.1016/j.ifacol.2021.08.407
34. Zhou, T., Kerschen, G.: Identification of secondary resonances of nonlinear systems using phase-locked loop testing. J. Sound Vib. **590**, 118549 (2024). https://doi.org/10.1016/j.jsv.2024.118549
35. Preumont, A.: Vibration control of active structures. Springer International Publishing, Cham (2018)
36. Anastasio, D., Marchesiello, S., Kerschen, G., Noël, J.P.: Experimental identification of distributed nonlinearities in the modal domain. J. Sound Vib. **458**, 426–444 (2019). https://doi.org/10.1016/j.jsv.2019.07.005
37. Touzé, C., Thomas, O., Huberdeau, A.: Asymptotic non-linear normal modes for large-amplitude vibrations of continuous structures. Comput. Struct. **82**, 2671–2682 (2004). https://doi.org/10.1016/j.compstruc.2004.09.003
38. Claeys, M., Sinou, J.J., Lambelin, J.P., Alcoverro, B.: Multi-harmonic measurements and numerical simulations of nonlinear vibrations of a beam with non-ideal boundary conditions. Commun. Nonlinear Sci. Numer. Simul. **19**, 4196–4212 (2014). https://doi.org/10.1016/j.cnsns.2014.04.008
39. Touzé, C., Amabili, M.: Nonlinear normal modes for damped geometrically nonlinear systems: application to reduced-order modelling of harmonically forced structures. J. Sound Vib. **298**, 958–981 (2006). https://doi.org/10.1016/j.jsv.2006.06.032